Solid Earth, 5, 837–849, 2014
www.solid-earth.net/5/837/2014/
doi:10.5194/se-5-837-2014

Solid Earth
Open Access

Exploring the shallow structure of the San Ramón thrust fault in Santiago, Chile (∼ 33.5° S), using active seismic and electric methods

D. Díaz[1,3], **A. Maksymowicz**[1,2], **G. Vargas**[2,3], **E. Vera**[1,3], **E. Contreras-Reyes**[1,3], **and S. Rebolledo**[2]

[1]Departamento de Geofísica, Facultad de Ciencias Físicas y Matemáticas, Universidad de Chile, Chile
[2]Departamento de Geología, Facultad de Ciencias Físicas y Matemáticas, Universidad de Chile, Chile
[3]Centro de Excelencia en Geotermia de los Andes (FONDAP-CEGA), Facultad de Ciencias Físicas y Matemáticas, Universidad de Chile, Chile

Correspondence to: D. Díaz (ddiaz@dgf.uchile.cl)

Received: 5 December 2013 – Published in Solid Earth Discuss.: 28 January 2014
Revised: 10 July 2014 – Accepted: 11 July 2014 – Published: 26 August 2014

Abstract. The crustal-scale west-vergent San Ramón thrust fault system, which lies at the foot of the main Andean Cordillera in central Chile, is a geologically active structure with manifestations of late Quaternary complex surface rupture on fault segments along the eastern border of the city of Santiago. From the comparison of geophysical and geological observations, we assessed the subsurface structural pattern that affects the sedimentary cover and rock-substratum topography across fault scarps, which is critical for evaluating structural models and associated seismic hazard along the related faults. We performed seismic profiles with an average length of 250 m, using an array of 24 geophones (Geode), with 25 shots per profile, to produce high-resolution seismic tomography to aid in interpreting impedance changes associated with the deformed sedimentary cover. The recorded travel-time refractions and reflections were jointly inverted by using a 2-D tomographic approach, which resulted in variations across the scarp axis in both the velocities and the reflections that are interpreted as the sedimentary cover-rock substratum topography. Seismic anisotropy observed from tomographic profiles is consistent with sediment deformation triggered by west-vergent thrust tectonics along the fault. Electrical soundings crossing two fault scarps were used to construct subsurface resistivity tomographic profiles, which reveal systematic differences between lower resistivity values in the hanging wall with respect to the footwall of the geological structure, and clearly show well-defined east-dipping resistivity boundaries. These boundaries can be interpreted in terms of structurally driven fluid content change between the hanging wall and the footwall of the San Ramón fault. The overall results are consistent with a west-vergent thrust structure dipping ∼ 55° E in the subsurface beneath the piedmont sediments, with local complexities likely associated with variations in fault surface rupture propagation, fault splays and fault segment transfer zones.

1 Introduction

The San Ramón Fault (SRF) is a kilometric crustal-scale west-vergent thrust fault system, located east of the highly populated city of Santiago, at the piedmont of the main Andean Cordillera of central Chile (Fig. 1). The SRF is a N–S fault situated along the eastern border of the Santiago central valley, formed by N–S to NNW-striking fault segments evidenced by conspicuous Quaternary fault scarps disrupting alluvial sediments of the piedmont units (Armijo et al., 2010). The SRF zone has been associated with compressive tectonics that raised the main Andean Cordillera with respect to the central valley of Santiago, likely since the Miocene in central Chile (Armijo et al., 2010; Farías et al., 2010; Rauld, 2011).

Recent tectonic activity has been evidenced through the analysis of 5 m high fault scarps affecting late Quaternary alluvial units (Fig. 1), according to structural-geomorphological work (Armijo et al., 2010; Rauld, 2011) and ongoing paleoseismological studies from trenches (Vargas and Rebolledo, 2012). Alluvial piedmont sediments in this area, located at around 800–900 m a.s.l. (meters above sea level), correspond mostly to coarse massive and poorly

Published by Copernicus Publications on behalf of the European Geosciences Union.

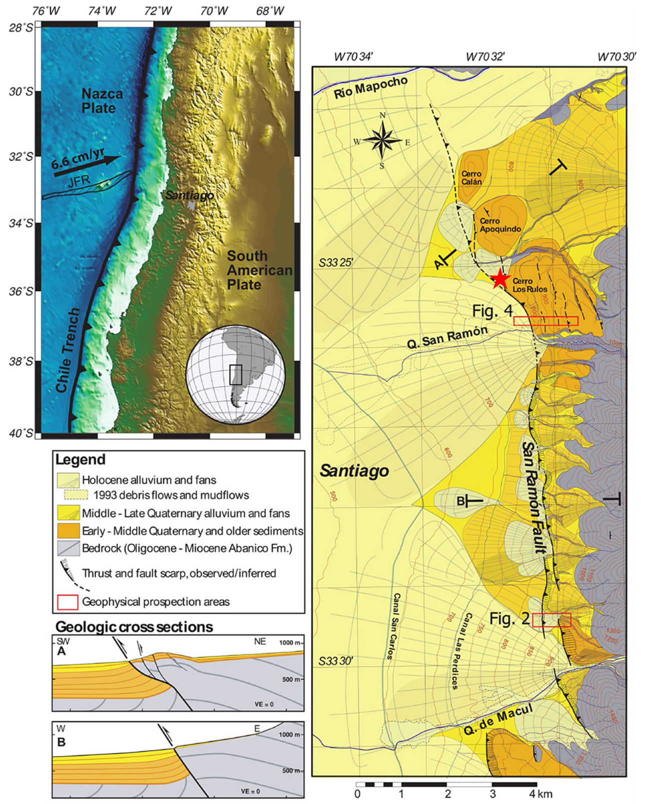

Figure 1. Geological chart (top left panel) and cross sections of the study zone showing the San Ramón fault system along the eastern border of Santiago (bottom left panels), and locations of the geophysical measurements (right panel) (modified from Armijo et al., 2010). Locations of geophysical measurements are marked by red rectangles, enclosing the areas shown in Fig. 2 (Quebrada de Macul area) and Fig. 4 (La Reina area). A red star marks the position of the Baños de Apoquindo spring.

sorted debris flow deposits and localized relatively well sorted lenses of channel-flow deposits in proximal areas of alluvial-fan geomorphologic units. These units are disposed at the foot of the mountain front, which constitutes the western limit of the main Andean Cordillera, composed mostly of Cenozoic volcanic rocks, reaching up to 3240 m a.s.l. at the San Ramón hill.

The objective of the study herein is to assess the subsurface surroundings of the SRF from the shallow velocity (V_p) structure using 2-D joint refraction and reflection seismic tomography (Korenaga et al., 2000). This method allows for direct inversion of the seismic velocities and thicknesses of a single layer when refractions and reflections are available. Refractions through the shallow sedimentary layer and reflections from the top of the volcanic rock substratum assigned to the Abanico Formation (Cenozoic) were registered, allowing for simultaneous calculation of velocities and substratum topography. Along with the active seismic experiment, electrical resistivity measurements along two profiles crossing fault scarps of the SRF provide us information on subsurface electrical properties at both sides of the fault zone. Determination of seismic velocities and electrical resistivity of the sedimentary layers above the substratum together with their behavior across the fault zone allows for improving the understanding about the geometry and Quaternary tectonics associated with the SRF in the eastern border of the highly populated city of Santiago.

Table 1. Specifications of the seismic experiment.

Profile	Orientation	Length [m]	Number of shots	Geophone spacing [m]
P1	W–E	269	27	5 and 10
P2	S–N	388	17	10
P3	S–N	373	17	10
P4	W–E	271	17	5

2 Geophysical measurements

2.1 Seismic experiment description

The seismic experiment was carried out in September–October 2011 and comprises four seismic lines. The purpose of the experiment was to detect small-scale structures with wavelengths smaller than 500 m, below one of the youngest fault scarps recognized along the SRF (Armijo et al., 2010). Thereby we employed a large number of shots with geophone spacing ranging from 5 to 10 m.

Figure 2 shows the location of the four seismic profiles (P1 to P4), which were designed so as to study the 5 m high fault scarp. The objective is to detect possible velocity changes from the west to the east of the scarp, which runs approximately N–S (Figs. 1 and 2). P1 and P4 cross the scarp axis, while P2 and P3 run parallel to the scarp axis, to the east and west of it, respectively (see Fig. 2b). Table 1 summarizes the experiment details. It is worth noting that there are urban roads and high-voltage towers in the east of the study area that limit the prolongation of the seismic lines further east (see Fig. 2a).

The seismic equipment employed comprises a 24-channel GEODE recorder, a seismic cable with a 10 m separation among channels and standard vertical geophones with a natural frequency of 14 Hz. Profiles P2, P3 and P4 were acquired by using a single streamer of 24 geophones for each profile, while data from profile P1 were obtained by two legs of 24 channels with an overlap section of 105 m. The topography used for our seismic modeling was provided by differential GPS data (Armijo et al., 2010; Rauld, 2011). As a seismic source, we used a 12 lb hammer hitting an iron sphere, which allowed us to record refractions imaging up to 50 m in depth and reflections mapping the top of the substratum at depths of 80–100 m.

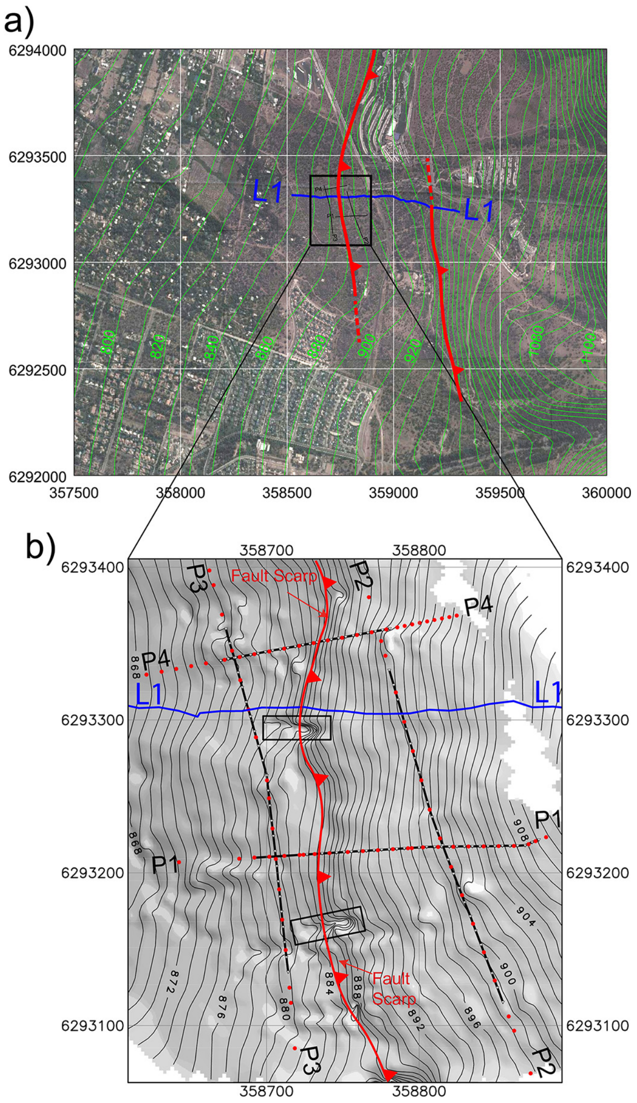

Figure 2. Location of seismic (P1–P4) and electric (L1) profiles at the Quebrada de Macul area. Green lines in **(a)** are contour lines of the topography based on SRTM data. Black lines in **(b)** are topographic contour lines based on D-GPS data, red dots mark shot locations and white triangles along black lines represent geophone positions. Black boxes mark the position of trenches used for ongoing paleoseismological studies in the area (Vargas and Rebolledo, 2012). Red line represents the approximate location of the SRF at the surface according Armijo et al. (2010). Coordinate system: UTM zone 19S, WGS84.

In order to generate a detailed tomography across the scarp, profiles P1 and P4 were measured using a geophone spacing of 5 m, except for the first four geophones of line P1, where a spacing of 10 m was used. However, since the north–south topographic gradients are small, profiles P2 and P3 were registered using a nominal geophone spacing of 10 m. These considerations allow recording of reflections from the top of the substratum. As a result of the dense vegetation in the studied zone, it was necessary to slightly change the direction of the seismic lines, which did not affect our 2-D modeling at the spatial-scale analysis.

2.2 *P*-wave velocity modeling

2.2.1 Forward modeling

In order to derive an initial model for the 2-D tomographic inversion, we first modeled the 1-D velocity structure for individual shots in each seismic profile. The 1-D velocity model consists of a combination of homogeneous and constant-velocity gradient layers in which thicknesses and top and bottom velocities can be interactively modified to adjust the travel times of different seismic arrivals seen in the data (Vera et al., 1990). Figure 3 shows examples of the seismic records associated with individual shots, including the predicted travel times from the 1-D model. One-dimensional models of each single shot registered in profiles P1 and P4 do not show significant variation concerning the velocity structure with depth across the lines. Hence for these two profiles we use the 1-D model of the shot showing the best signal (Fig. 3a and f) as a reference to build the initial model of the 2-D tomographic inversion. However, the 1-D models calculated using the shots located near the ends of the lines P2 and P3 show variations in the velocity structure with depth in the north–south direction (see Fig. 3b and c for the profile P2, and Fig. 3d and e for the line P3). Therefore we use two 1-D models in each profile as a reference for generating initial models for the 2-D inversion.

2.2.2 2-D travel-time inversion

We obtained the *P*-wave velocity–depth structure based on the joint refraction and reflection travel-time inversion method of Korenaga et al. (2000). This method allows joint inversion of seismic refraction and reflection travel-time data for a 2-D velocity field. Travel times and ray paths are calculated using a hybrid ray-tracing scheme based on the graph method and the local ray-bending refinement (van Avendonk et al., 1998). Smoothing constraints using predefined correlation lengths and optimized damping constraints for the model parameters are employed to regularize an iterative linearized inversion (Korenaga et al., 2000).

The 2-D initial models are based on the 1-D forward modeling previously calculated (see Sect. 2.2.1). A digital elevation model was obtained from topographic data resulting from D-GPS (Differential GPS) measurements taken in the area. The top of the substratum and the sedimentary velocities are jointly inverted using refractions through the sediment layer (P_s) and reflections from the top of the substratum (PbP). The horizontal grid spacing of the model used for the velocity inversion is 1 m, whereas the vertical grid spacing varied from 0.2 m at the top of the model to 0.5 m at its bottom. The selected values of grid spacing correspond to a

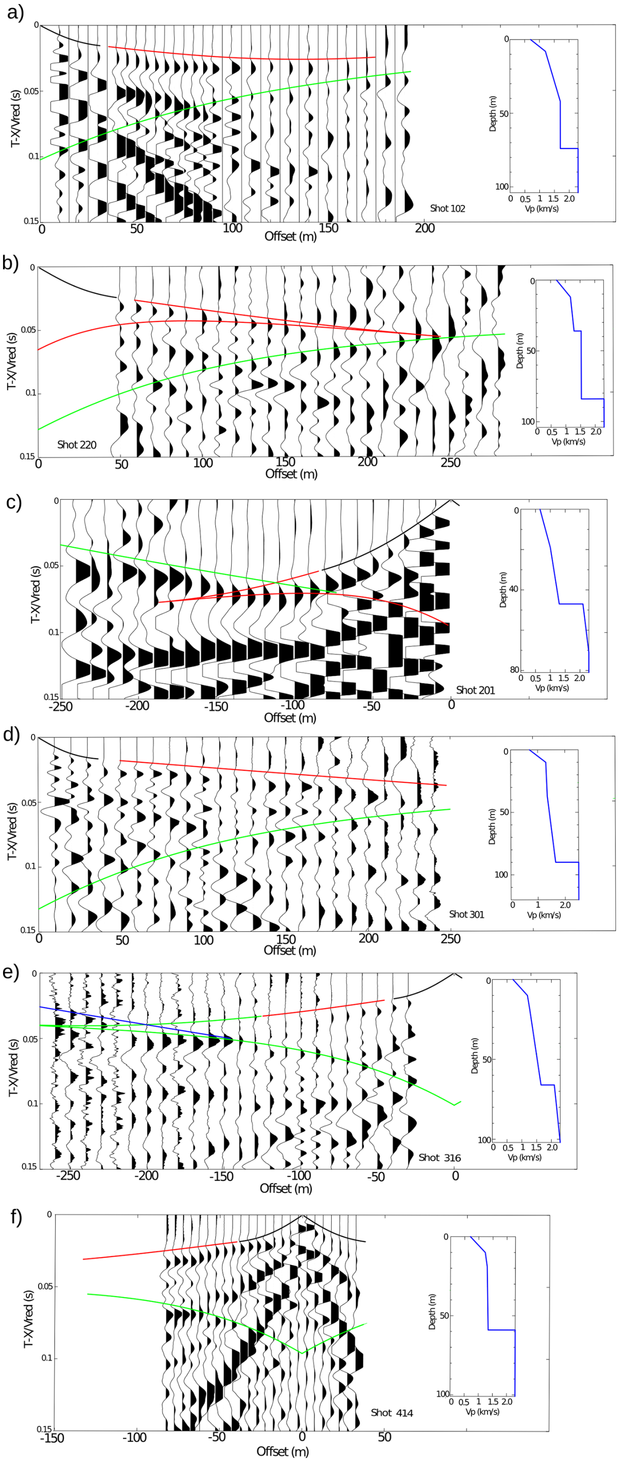

Figure 3. (a) Shot at −10 m, profile P1. **(b)** Shot at −50 m, profile P2. **(c)** Shot at 240 m, profile P2. The reduction velocity is 1.5 km s^{-1}, and the horizontal coordinate is shot–geophone distance (offset). **(d)** Shot at −10 m, profile P3. **(e)** Shot at 260 m, profile P3 **(f)** Shot at 82.5 m, profile P4. The reduction velocity is 1.5 km s^{-1}, and the horizontal coordinate is shot–geophone distance (offset).

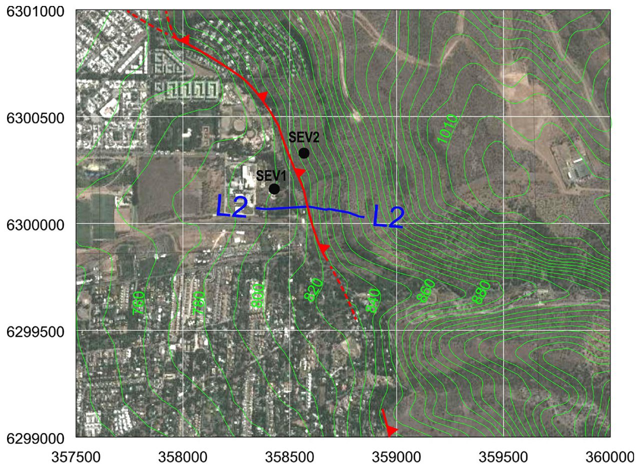

Figure 4. Location of electric profile L2 in the La Reina area. Topographic contour lines (green lines) are based on SRTM data. Points marked as SEV1 and SEV2 are two vertical electric soundings measured on the eastern and western sides of the SRF scarp observed in the area. Red line represents the approximate location of the SRF at the surface according Armijo et al. (2010). Coordinate system: UTM zone 19S, WGS84.

scaling of the values used by Korenaga et al. (2000) from large to small scale, which are on the scale of kilometers. Depth nodes defining the reflector for the joint inversion (top of the substratum) are spaced 5 m apart. We used horizontal correlation lengths (average-smoothness window) ranging from 0.5 m at the top to 2 m at the bottom of the model, and vertical correlation lengths varying from 0.2 m at its top to 1 m at its bottom. Different tests showed that varying the values of correlation lengths by 50 % does not significantly affect the results. As a result of the trade-off between correlation lengths and smoothing weights, we tried to apply shorter correlation lengths and larger smoothing weights to reduce memory requirements (Korenaga et al., 2000; Contreras-Reyes et al., 2008). Depth and velocity nodes are equally weighted in the refraction and reflection travel-time inversions. Table 2 summarizes the details regarding the final velocity model inverted. Figures 5b, 6b, 7b and 8b present the ray coverage for each seismic line, which provides an explicit resolution visualization of the seismic experiment.

2.3 Electrical resistivity measurements

DC (direct current) geoelectrics is one of the earliest geophysical exploration techniques, going back to the first decades of the last century. In short, it consists in feeding a current into the ground and measuring the resulting voltage drop. Vertical electrical sounding (VES) is perhaps the most commonly used strategy in the application of DC electrical methods.

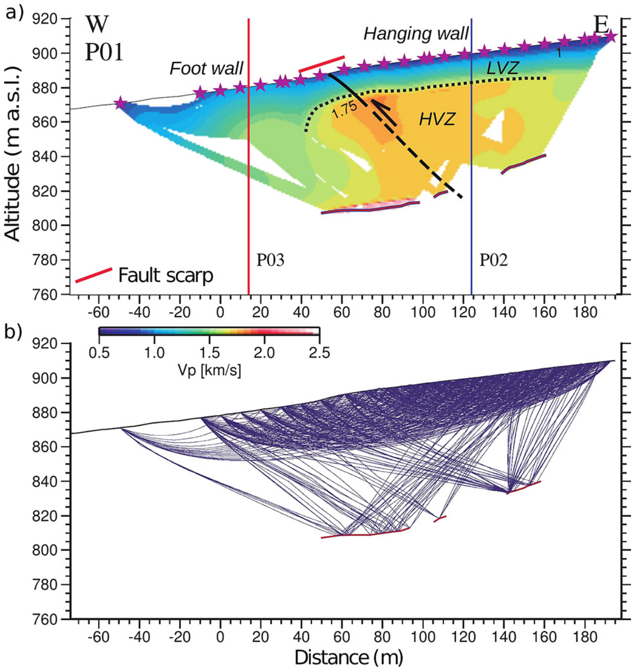

Figure 5. Results of seismic profile P1. **(a)** Final velocity model including the inverted reflector (blue line). Stars represent shot positions. Zero distance represents position of the first geophone along the profile. Solid black line represent the SRF system derived from paleoseismological studies (Vargas and Rebolledo, 2012), while dashed black lines are inferred structures related to the SRF. Dotted black line represents shallow sedimentary units. The intersections between P1 with profiles P3 and P2 are also indicated (see Fig. 2). **(b)** Associated ray paths.

The VES is based on the concept that the electrical structure of the Earth can be described by a one-dimensional resistivity function, $\rho = \rho(z)$, with the resistivity of a rock varying only with depth within the Earth. Assuming that the lateral change in resistivity of the Earth described by $\rho = \rho(x, y)$ is so slow at any one location, the profile $\rho(z)$ can be determined independently of the lateral variations, $\rho(x, y)$. Then, the lateral changes can be determined by a series of vertical electric soundings made along a profile, or over an area, and interpreted as a set of slowly changing $\rho(z)$ functions. For more details on VES, see Zhdanov (2009).

In practice, a VES consists of the injection of a current through two electrodes connected to the ground and the measurement of the corresponding electrical potential through a different pair of electrodes following a symmetrical setting (e.g., Wenner, Schlumberger, etc.). The concept of sounding relates to the increment of the current electrode spreading, which allows the inference of the electrical properties of the deeper layers of the studied zone. The use of Schlumberger settings for determining the subsurface resistivities is widespread in geophysical applications, mainly because of its simplicity and speed of survey.

Table 2. Summary of travel-time picks and details of the average final velocity–depth model shown in Figs. 5–8. The nomenclature is as follows: Ps (refractions), PbP (reflections from the top of the substratum), ΔT (average travel-time uncertainty), and TRMS (root-mean-square travel–time misfit).

Profile	Ps (T) [ms]	PbP (T) [ms]	Ps (TRMS) [ms]	Ps+PbP (TRMS) [ms]
P1	5	10	3.42	5.15
P2	5	10	4.81	4.68
P3	5	10	5.57	5.49
P4	5	10	4.31	4.80

Table 3. Specifications of the ERT measurements.

Profile	Orientation	Length [m]	Electrode spacing [m]
L1	W–E	840	7
L2	W–E	560	7

During our work, an instance of 2-D electrical resistivity imaging was performed along with the normal VES measurements. Electric resistivity tomography (ERT) is a proven imaging technique and both its theory and application are well documented in geophysical research literature (e.g., Griffiths and Barker, 1993). It has been proven that ERT is a useful tool in mineral exploration, as well as in hydrogeology or exploration of sedimentary basins (e.g., Colella et al., 2004; Brunet et al., 2010; Zarroca et al., 2011).

2.4 Data acquisition and processing for ERT measurements

The multi-electrode resistivity technique uses multi-core cables (ABEM SAS 1000 unit) with as many conductors (between 81 and 121 in this study) as there are electrodes plugged into the ground at fixed spacing. The two-location survey was carried out using a symmetric Wenner–Schlumberger configuration. The unit electrode spacing was 7 m along both profiles (see Table 3). Profile L1 was measured using three segments of 560 m each. The overlap was of 420 m, and the total length was 840 m. Profile L2 was measured as a single segment of 560 m. The location of both profiles can be seen in Figs. 2 and 4.

To calculate the resistivity of the material, the electrical potential difference created by an electrical current passing through the ground via the conductors is measured. The different combination of current and potential pairs of electrodes results in the mixed sounding and profiling section with the corresponding maximum depth of investigation, which in turn depends on the length of the cable and the type of configuration used for the survey. The changes of resistivity related to depth allow the construction of a 2-D section of the subsurface resistivity values.

These data were inverted using the RES2DINV inversion routine, which uses a nonlinear smoothness-constrained least-squares technique to calculate the resistivity of the model blocks (de Groot-Hedlin and Constable, 1990; Sasaki, 1992; Loke et al., 2003), and a finite-element approach to generate apparent resistivity values. An optimization process tries to iteratively reduce the difference between the calculated and measured apparent resistivity values. The percentage error, considering N points of comparison for each data set, was calculated as a data fit indicator. For a comparison of measured and calculated apparent resistivity pseudosections along profiles L1 and L2, see the Appendix (Figs. A3 and A4).

3 Results

4 Seismic measurements

The 1-D velocity–depth models (Fig. 3) provide key information to define the general structure of the sedimentary layer. These models show typical sedimentary velocities with moderate compaction ($V_\mathrm{p} < 2\,\mathrm{km\,s^{-1}}$). A shallow layer with $V_\mathrm{p} \sim 0.7\,\mathrm{km\,s^{-1}}$ is observed, probably made of soft soil and poorly compacted sediments. Deeper, the 1-D models show an increase of velocity indicating the increase of sediment compaction. A strong velocity discontinuity detected in the 1-D velocity models was interpreted as a reflector associated with the sedimentary cover–volcanic rock substratum interface. The modeled reflector becomes systematically shallower to the north (perpendicular to the direction of the topographic gradient in the region) as it is observed in Fig. 3. This geometry change in the substratum-reflector topography is clearer in the 2-D tomographic models (Figs. 5–8), but it is remarkable that the simple 1-D modeling provides information about its shape's differences.

The 2-D velocity–depth models present more detailed images, including topographic effects and velocity heterogeneities (Figs. 5–8). The latter was possible due to the large number of shots and the narrow spacing between geophones in accordance with the spatial scale of the analysis (1–100 m). The main observations from the 2-D tomographic profiles are described in the rest of this section.

P1 and P4 (Figs. 5 and 6): both profiles cross the fault scarp in an approximately E–W direction. In profile P1 (Fig. 5), located in the southern part of the study area, the velocity–depth model shows a decrease in the vertical gradient of velocity marked by the iso-velocity contour of $1.5\,\mathrm{km\,s^{-1}}$ (segmented red line in Fig. 5a). This change is interpreted as the transition from a poorly compacted shallower sedimentary unit to a more competent layer at depth. The location of the SRF from paleoseismological studies in trenches (Vargas and Rebolledo, 2012) is indicated by a continuous black line. In the hanging wall of the SRF fault scarp the interpreted shallower sedimentary unit shows a homogenous thickness and internal velocity gradient, while in the footwall this unit becomes thicker and its internal vertical gradient of velocity decreases. A localized deepening of the iso-contours of velocities at $x \sim 40\,\mathrm{m}$ in the footwall of the fault scarp suggests a complexity in the subsurface soil structure that could be associated with another fault. The deepest reflector (blue line), interpreted as the change between sedimentary cover and substratum rocks, shows a similar inclination with respect to the topography. The eastward shallowing of this interpreted substratum could be related to the presence of the SRF, but the distribution of the reflected rays does not allow for its shape to be properly defined with a high enough resolution to support this hypothesis (Fig. 5b).

Profile P4 is parallel to P1 and it is located in the northern part of the study area. Seismic velocities along P4 (Fig. 6a) are similar to those observed along P1. The iso-velocity contour of $1.5\,\mathrm{km\,s^{-1}}$ becomes remarkably deeper to the west. A localized deepening of the iso-contours of velocities at $x \sim 40\,\mathrm{m}$ suggests, as in profile P1, local complexity that could be associated with another thrusting. The sediment–substratum interface was detected only by reflections in the central portion of the profile (Fig. 6b), but its trend indicates a relatively constant depth of $\sim 70\,\mathrm{m}$ below the topography. The smooth shape of the substratum, well defined by reflections, suggests that this is not cut by the SRF in this short segment of the profile P4. For more details on the estimation of the substratum depth, see the Appendix (Fig. A2).

P2 and P3 (Figs. 7 and 8): both profiles are located parallel to the fault scarp. Profile P2 (Fig. 7) is located to the east of the scarp, in the hanging wall of the observed fault at the surface and it strikes in an approximately N–S direction. The velocity–depth model is well explained by a combination of flat layers (1-D) with a slight increase in velocities around $x = 40\,\mathrm{m}$ (Fig. 7a). The main feature of this model is the clear reduction in depth of the reflector around a distance of 80 m along the profile. This observation is well constrained by the distribution of reflected rays which support a smooth deepening to the south of the substratum.

Profile P3 (Fig. 8) is located to the west of the scarp, in the footwall of the observed fault at the surface, and like P2 it is well represented by a simple combination of flat layers that present a local increase in velocities around 80 m distance along the profile. The slight variations seen along profiles P2 and P3 can be explained by differences in the amount and compaction of sedimentary flows sourced mainly from the east. Similar to P2, the velocity depth model along P3 shows a southward deepening of the substratum with a 20 m variation in depth between the southern and northern segments of the profile.

4.1 Resistivity measurements

ERT experiments resulted in two profiles, one crossing the late Quaternary fault scarp of the SRF where seismic profiles were realized (L1, Quebrada Macul area, Fig. 2), and one

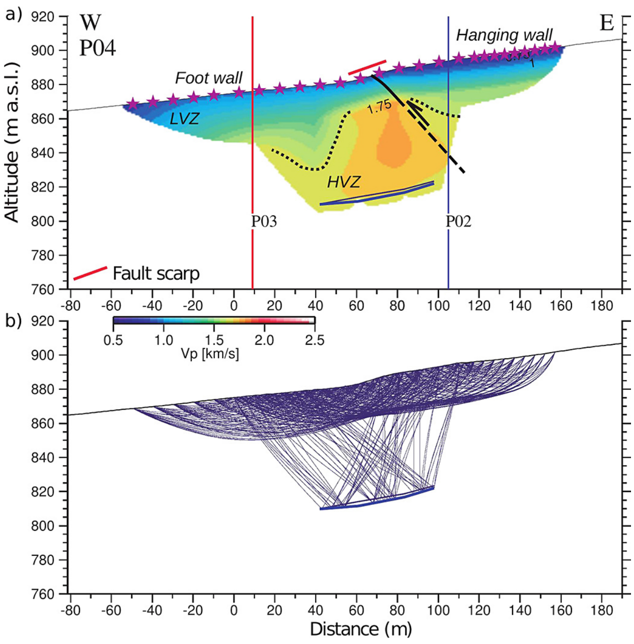

Figure 6. Results of seismic profile P4. **(a)** Final velocity model including the inverted reflector (blue line). Stars represent shot positions. Zero distance represents position of the first geophone along the profile. Black line represent the SRF derived from paleoseismological studies (Vargas and Rebolledo, 2012), while dashed black lines are inferred structures related to the SRF. Dashed red line represents shallow sedimentary units. The intersections between P4 with profiles P3 and P2 are also indicated (see Fig. 2). **(b)** Associated ray paths.

crossing a more evolved fault scarp which probably represents a longer history of the SRF during the Quaternary (L2, La Reina area, Fig. 4). The inversion of ERT data along the L2 profile resulted in a model with resistivity values between 1 and 600 Ωm (see Fig. 9), and a percentage error of 4.4 % between measured and modeled data (see Fig. A3 of the Appendix). The resistivity distribution in this profile shows clearly two different areas. The western part, from 0 to 280 m horizontally, presents much higher resistivity values (100–600 Ωm) compared with the eastern part of the profile (280–530 m), where the observed resistivity values were as low as 5–50 Ωm. The resistivity contrast at 280 m clearly appears in the ERT section. This change can be observed at depth in this profile, defining a sharp lateral resistivity contrast zone dipping 60–54° E, which can be interpreted as structural control on electric properties associated with the SRF.

Two VESs using the Schlumberger array (200 m maximum spread) were carried out in the eastern and western part of the L2 profile (Fig. 4) in order to check the strong resistivity discontinuity observed there. The results confirmed the observations from profile L2, with resistivity values between 100 and 200 Ωm in the western part of the profile and of 10–20 Ωm at its eastern part (see Appendix, Fig. A5).

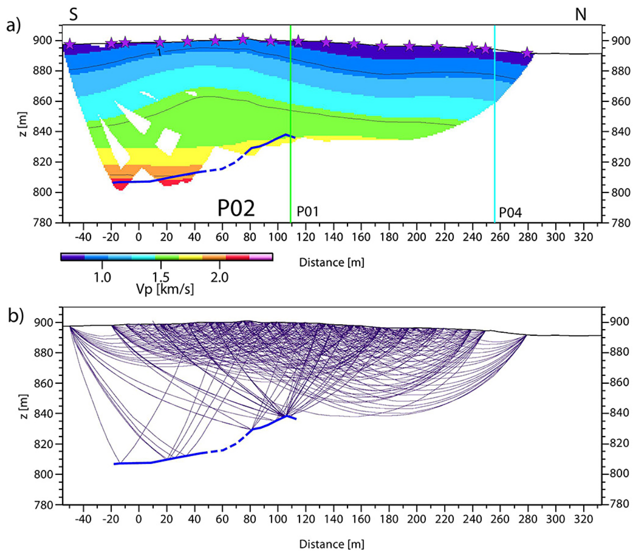

Figure 7. Results of seismic profile P2. **(a)** Final velocity model including the inverted reflector (blue line). The segmented blue line indicates the regions where the reflector is poorly constrained. Stars represent shot positions. Zero distance represents position of the first geophone along the profile. The intersections between P2 with profiles P1 and P4 are also indicated (see Fig. 2). **(b)** Associated ray paths.

The inversion of ERT data along the L1 profile resulted in a model with a percentage error of 2.8 % (see Fig. 10, and A4 of the Appendix). The resistivity distribution along this profile presents in general larger values in shallow layers with respect to deeper layers of the model (high- and low-resistivity units, respectively; Fig. 10). At 220 m horizontal distance from the western border of this profile, a relatively low resistivity structure penetrates from the lower resistivity unit into the shallow layer of high-resistivity values, defining a local low-resistivity zone dipping around 55° E (Fig. 10). This change matches the observed fault in the young fault scarp of the SRF at the surface (Figs. 2 and 10). Similar features with more conductive zones interrupting the continuity of the shallow high-resistivity unit can be observed at 130 and 350 m from the western border of this profile, suggesting additional secondary structures. In the easternmost part of this profile (740 m from the western border, right-hand side in Fig. 10), it is possible to observe a sharp lateral contrast in low and high-resistivity values dipping to the east, similar to profile L2 and also located in a more evolved fault scarp, which could be associated with a different segment of the SRF in this area (Fig. 4). For apparent resistivity pseudosections along profiles L1 and L2, see the Appendix (Figs. A3 and A4).

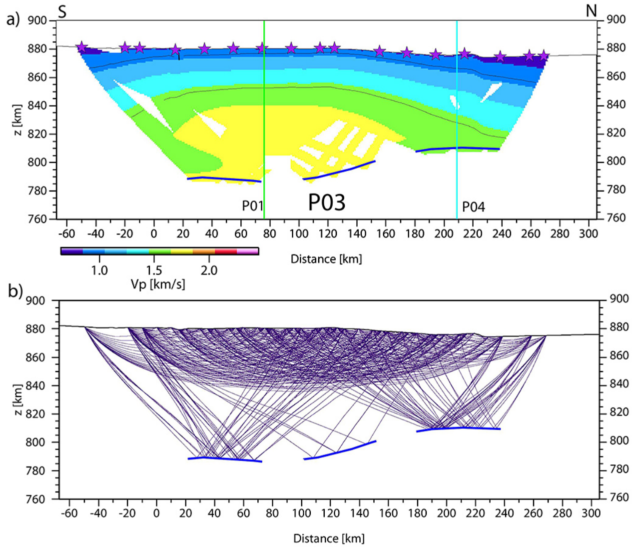

Figure 8. Results of seismic profile P3. **(a)** Final velocity model including the inverted reflector (blue line). Stars represent shot positions. Zero distance represents position of the first geophone along the profile. The intersections between P3 with profiles P1 and P4 are also indicated (see Fig. 2). **(b)** Associated ray paths.

5 Discussion

Active seismic and electric methods provided complementary data for exploring changes in the subsoil structure along the eastern border of the city of Santiago. The substratum depth obtained along each seismic profile, around 70 m below the surface topography, is consistent in the four intersection points with an error of ±10 m. The comparison of seismic velocities between the different profiles at the four intersection points indicated seismic anisotropy of about 50 % (difference of 0.3–0.8 $\mathrm{km\,s^{-1}}$), which evidences that the stress field in the region is not isotropic, especially along the east–west direction.

Seismic models in profiles P1 and P4 (oriented E–W) show substratum surface approximately parallel to the surface topography with a slight reduction in depth to the east (Figs. 5 and 6). The increase in velocities with depth is faster in the hanging wall (eastward) with respect to those in the footwall (westward) of the observed fault at the surface, indicating a relative higher compaction to the east of the structure (Fig. 2). This E–W change in vertical V_p gradients in the western side with respect to the eastern side of the fault scarp can be interpreted like the result of thicker poorly compacted alluvial sediments in the footwall with respect to the hanging wall of the fault, and could be associated with the development of a syntectonic basin resulted from late Quaternary kinematics along the SRF. Thus, the overall observations are consistent with sedimentary units deformed by an inverse west-vergent fault at subsurface levels. In addition, the substratum geometry interpreted from the seismic experiments suggests that at deep levels (∼ 60–80 m), the San Ramón fault presents north–south variations, probably associated with fault transfer zones, and that this structure could strike NNW, as indicated by the abrupt change in the depth of the substratum observed in profiles P2 and P3, from which a ∼30° N westward-striking structure may be deduced. In addition, these variations in substratum depth along profiles P2 and P3 could be also associated with erosional surfaces produced by ancient streams of from the main quebradas in the area.

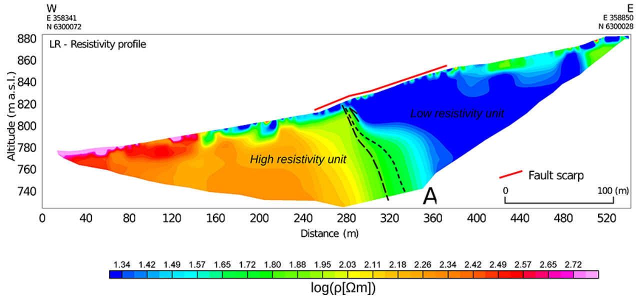

Figure 9. Inversion result along the La Reina (L2) profile, including main structures interpreted in the text. Resistivity values show a strong contrast between the eastern (conductive) and western (resistive) part of the profile.

The electrical resistivity values obtained from two profiles crossing the San Ramón fault zone vary from 10 to 800 Ωm. The L2 profile shows a strong lateral variation, with values of 10–20 Ωm on the eastern side of the fault zone, interpreted close to the base of the fault escarpment, and 100–200 Ωm at its western side. The effect of porosity and fluid presence in the electrical resistivity of rocks has been widely observed, particularly in sedimentary environments and also in fault zones (e.g., Caputo et al., 2007; Colella et al., 2004; Unsworth et al., 2000), confirming the strong correlation between fluid presence in highly porous media and high (electrolytic) conductivity. As water content is one of the parameters that strongly control the resistivity both in sedimentary layers and in fractured substratum rocks, this difference could be related to diminished permeability at the fault core zone, acting as a barrier for fluids possibly due to localized slip along the fault planes at shallower levels (Caine et al., 1996) as well as a lithological change with shallower substratum in the hanging wall with respect to the footwall of the fault. This could cause a zone of low resistivity by trapping groundwater uphill of the fault zone keeping the sedimentary alluvial layers dryer in the footwall due to a sharp drop of the water table, which results in higher resistivity values immediately to the west of the geologic structure. The influence of the SRF in the water control and transport down to the valley can be also inferred from the location of the Baños de Apoquindo spring (see Fig. 1), very close to the fault scarp in that area.

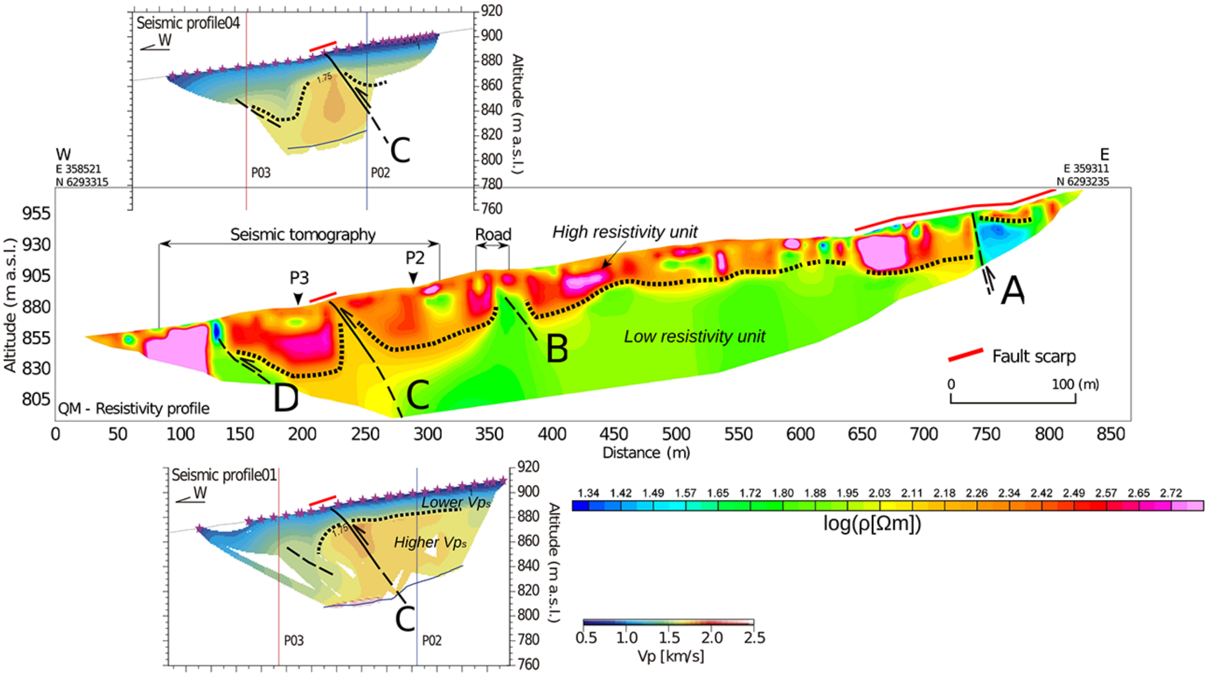

Figure 10. Inversion result close to along the Quebrada de Macul (L1) profile, including main structures interpreted in the text. Lower resistivity values at depth tend to remain on the eastern side of the profile. Note that the structure marked as A could be the same structure observed in both zones (see Fig. 9). Results from seismic profiles P01 and P04 have been added for comparison. See zoomed view of P04 together with a corresponding outcrop from ongoing paleoseismological studies in Fig. 11.

A similar behavior can be interpreted from the L1 profile, where lower resistivity values at depth tend to remain on the eastern side of the profile, while on the western side there is scarcely any conductivity increment with depth, which can be interpreted like structural control on the groundwater system resulting in systematically higher water tables in the hanging wall with respect to the footwall of the structures. Besides, four prominent features are observed along profile L1. In the easternmost part of this profile, a sharp lateral resistivity change can be interpreted as a structure dividing zones with high (downhill) and low (uphill) resistivity values below 30 m depth, similar to the structure interpreted from the L2 profile; in both cases those structures are located at the base of the main topographic fault escarpments associated with the San Ramón fault ("A" in Figs. 9 and 10). The westernmost structures observed in profile L1 ("C" and "D" in Fig. 10) are characterized by relatively increased conductivity, which probably reflects localized increased permeability resulting from recent surface ruptures along faults in the area, in accordance with complexities that characterize permeability changes in fault zones (Caine et al., 1996). One of those structures ("C", Fig. 10) corresponds to an observed fault affecting recent sediments according to ongoing paleoseismological studies (Vargas and Rebolledo, 2012), showing a remarkable association with shallow seismic results as well (see Fig. 11). If the reflection located around 70 m below the surface topography here is effectively associated with the volcanic-rock-substratum–sedimentary-cover transition (P4, Fig. 10), it is possible for it to be interpreted that the low-resistivity unit characterizes relatively humid sediments confined below a dry surface sediment layer of about 50 m thickness at the location of the young fault scarp, and above a highly fractured substratum characterized by higher V_p and lower electrical resistivity (Fig. 10).

The comparison between the paleoseismological trench with the seismic and resistivity tomographic profiles (Figs. 10 and 11) reveals a change in the dip of the fault between the most surface levels and deeper zones. The fault was observed dipping 17–20° E at surface (Fig. 11), but it quickly evolves to a fault dipping around 55° at depths greater than 10–20 m, according to our interpretation from the seismic and resistivity profiles (Figs. 10 and 11), in agreement with the dominant dip of the SRF proposed by Armijo et al. (2010). Similarly, other inferred structures ("D" and "B") shown in L1 (QM-resistivity profile, Fig. 10) could be associated with local complexities like fault splay and fault segment transfer zones (Figs. 1 and 2).

The change in fault-dip pattern observed at the surface level in trenches (17–20° E), with respect to deeper subsurface levels inferred from geophysics and structural observations (ca. 55° E in general, Fig. 11), have been typically described from paleoseismological results in active reverse structures, associated with collapse, overthrusting and plastic

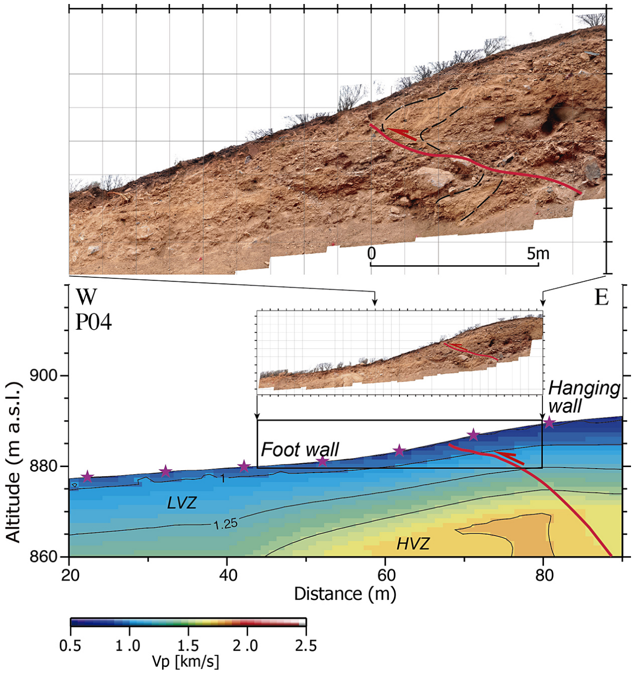

Figure 11. Surface observation of a fault affecting recent sediments close to seismic profile P04, from ongoing paleoseismological studies (Vargas and Rebolledo, 2012), together with a zoomed view of the results obtained along this profile.

deformation of the hanging wall close to the soil surface during earthquakes (McCalpin and Carver, 2009).

6 Conclusions

We interpreted seismic and resistivity profiles across one of the youngest and evolved Quaternary escarpments of the San Ramón Fault, which evidenced clearly localized V_p and resistivity changes at the subsurface associated with main and secondary structures. Seismic and electric models are consistent with sedimentary units deformed by reverse west-vergent localized faults, dipping around 55° E at depth, cutting the piedmont sedimentary cover and substratum rocks, and possibly controlling the position of the water table in the eastern border of the Santiago valley. The geophysical observations also suggest local complexities that can be associated with fault splay or fault segment transfer zones.

Given the acute urbanization on the eastern border of the city of Santiago, future measurements should focus on a better coverage along the fault zone through geophysical techniques, which together with detailed paleoseismological and geomorphological results will improve critical knowledge concerning the geometry, Quaternary kinematics and potential seismic hazard related to the San Ramón Fault. This information will be extremely valuable for implementation of better territorial planning in the continuously growing city of Santiago.

Appendix A

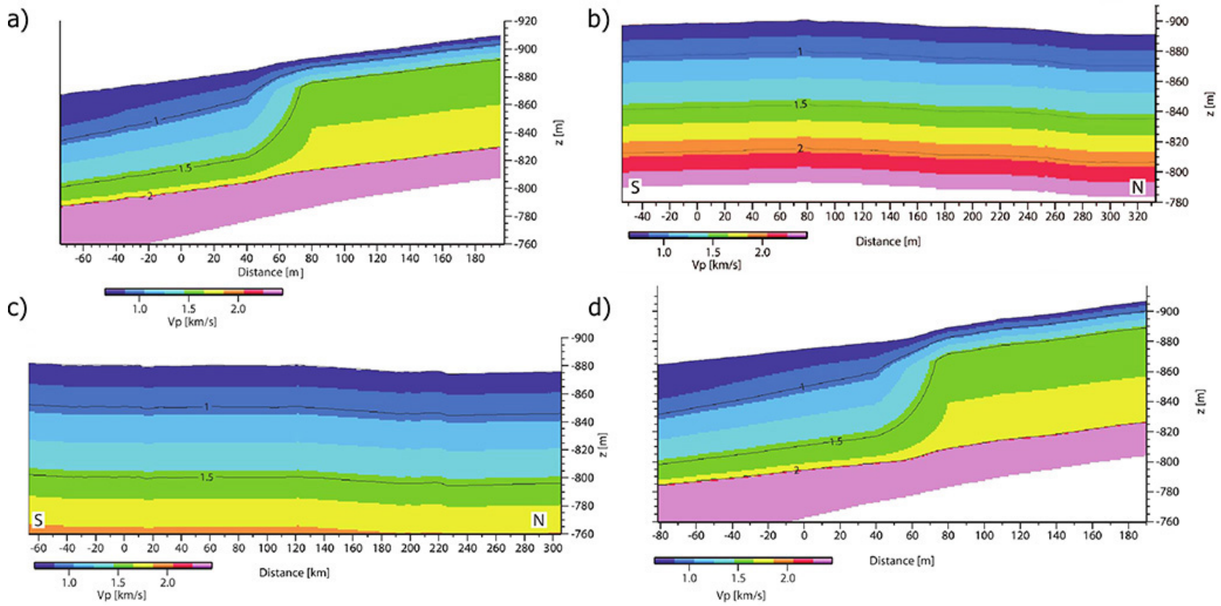

Figure A1. Initial velocity models for profiles **(a)** P1, **(b)** P2, **(c)** P3 and **(d)** P4.

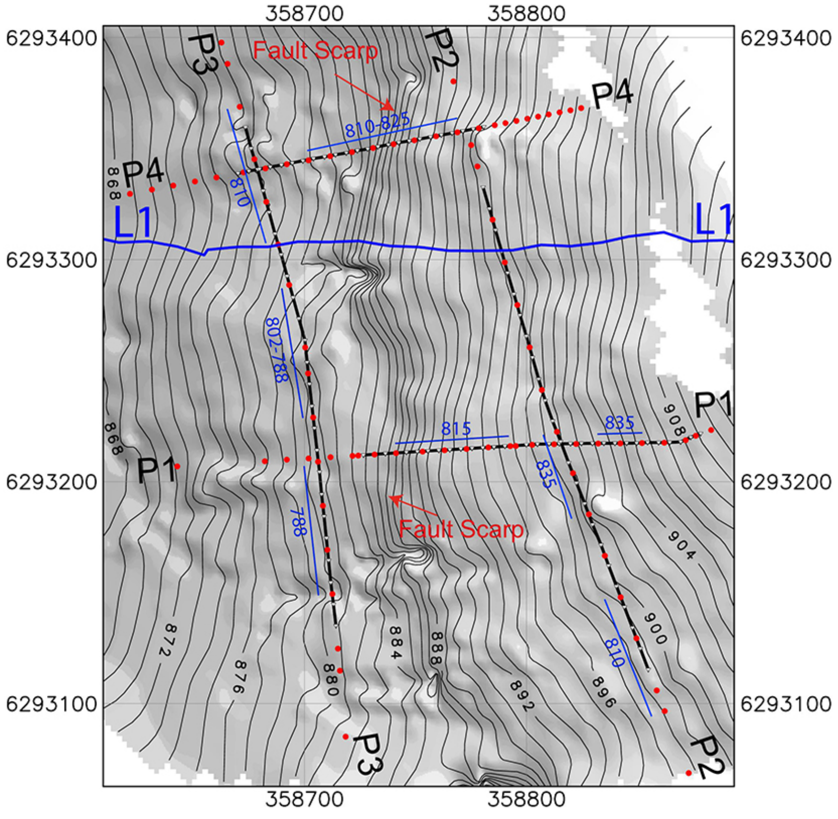

Figure A2. Estimated substratum depth [m]. Blue lines along seismic profiles P1–P4 mark the substratum depth, based on the 2-D seismic velocities models.

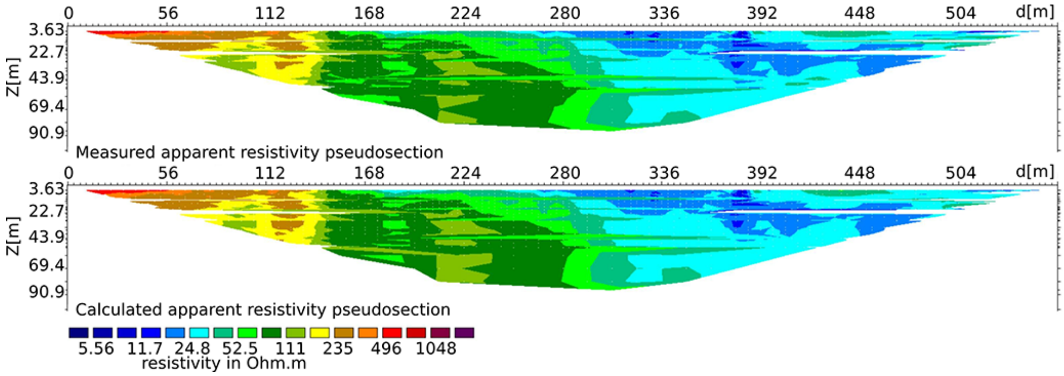

Figure A3. Apparent resistivity pseudosections. Measured (top) and obtained from inversion (bottom) apparent resistivity pseudosections along L2 profile.

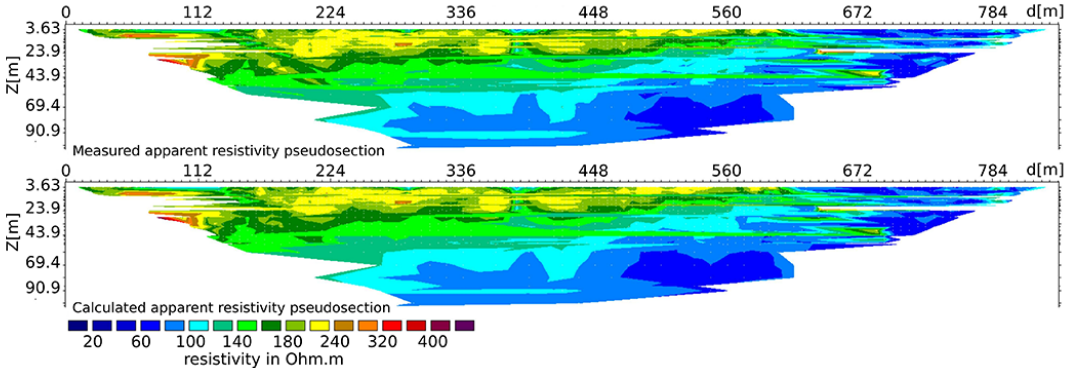

Figure A4. Apparent resistivity pseudosections. Measured (top) and obtained from inversion (bottom) apparent resistivity pseudosections along L1 profile. Two VESs were carried out using a Schlumberger configuration approximately 100 m on the eastern and western sides of the San Ramón fault scarp observed in that area.

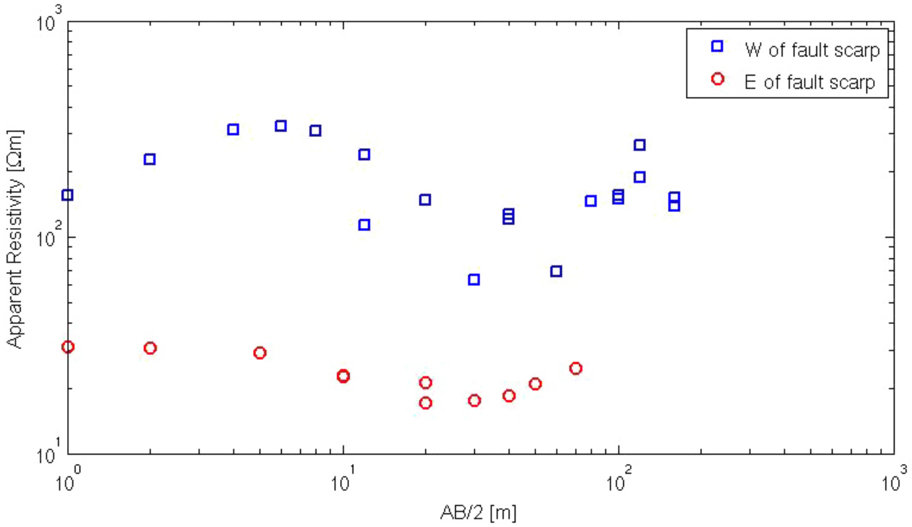

Figure A5. VES close to L2 profile. The results of both VESs are shown in this figure as blue squares for apparent resistivity on the western side of the fault scarp (SEV1 in Fig. 4) and red circles on the eastern side of the fault scarp (SEV2 in Fig. 4).

The Supplement related to this article is available online at doi:10.5194/se-5-837-2014-supplement.

Acknowledgements. We thank C. Gómez and K. Garcia for their assistance on the fieldwork.

ERT measurements, data processing and 2-D inversions of ERT data were carried out by Wellfield Services Ltda.

This work was supported by the Ministerio de Vivienda y Urbanismo (project no. 640-27-LP10) and the Comisión Chilena de Energía Nuclear (project no. CHI9020) in the frame of research programs developed by the Departamento de Geología and the Departamento de Geofísica, Facultad de Ciencias Físicas y Matemáticas, Universidad de Chile. We are grateful for the additional support from CEGA (Andean Geothermal Center of Excellence, Fondap, project no. 15090013).

Edited by: W. Geissler

References

Armijo, R., Rauld, R., Thiele, R., Vargas, G., Campos, J., Lacassin, R., and Kausel, E.: The West Andean Thrust, the San Ramón Fault, and the seismic hazard for Santiago, Chile, Tectonics, 29, TC2007, doi:10.1029/2008TC002427, 2010.

Brunet, P., Clément, R., and Bouvier, C.: Monitoring soil water content and deficit using Electrical Resistivity Tomography (ERT) – A case study in the Cevennes area, France, J. Hydrol., 380, 146–153, 2010.

Caine, J. S., Evans, J. P., and Forster, C. B.: Fault zone architecture and permeability structure, Geology, 24, 1025–1028, 1996.

Caputo, R., Salviulo, L., Piscitelli, S., and Loperte, A.: Late Quaternary activity along the Scorciabuoi Fault (Southern Italy) as inferred from electrical resistivity tomographies, Ann. Geophys.-Italy, 50, 213–224, 2007.

Colella, A., Lapenna, V., and Rizzo, E.: High-resolution imaging of the High Agri Valley Basin (Southern Italy) with electrical resistivity tomography, Tectonophysics, 386, 29–40, 2004.

Contreras-Reyes, E., Grevemeyer, I., Flueh, E. R., Scherwath, M., and Bialas, J.: Effect of trench-outer rise bending-related faulting on seismic Poisson's ratio and mantle anisotropy: a case study offshore of southern central Chile, Geophys. J. Int., 173, 142–156, doi:10.1111/j.1365-246X.2008.03716.x, 2008.

de Groot-Hedlin, C. and Constable, S.: Occam's inversion to generate smooth, two-dimensional models from magnetotelluric data, Geophysics, 55, 1613–1624, 1990.

Farías, M., Comte, D., Charrier, R., Martinod, J., David, C., Tassara, A., Tapia, F., and Fock, A.: Crustal-scale structural architecture in central Chile based on seismicity and surface geology: Implications for Andean mountain building, Tectonics, 29, TC3006, doi:10.1029/2009TC002480, 2010.

Griffiths, D. H. and Barker, R. D.: Two-dimensional resistivity imaging and modelling in areas of complex geology, J. Appl. Geophys., 29, 211–226, 1993.

Korenaga, J., Holbrook, W. S., Kent, G. M., Kelemen, P. B., Detrick, R. S., Larsen, H. C., Hopper, J. R., and Dahl-Jensen, T.: Crustal structure of the southeast Greenland margin from joint refraction and reflection seismic tomography, J. Geophys. Res., 105, 21591–21614, 2000.

Loke, M. H., Acworth, I., and Dahlin, T.: A comparison of smooth and blocky inversion methods in 2D electrical imaging surveys, Explor. Geophys., 34, 182–187, 2003.

McCalpin, J. P. and Carver, G.: Paleoseismology of Compressional Tectonic Environments, in: Paleoseismology, edited by: McCalpin, J. P., Academic Press (Elsevier), International Geophysical Series, 95, 315–419, 2009.

Rauld, R.: Deformación cortical y peligro sísmico asociado a la falla San Ramón en el frente cordillerano de Santiago, Chile central (33° S), Ph.D. thesis, Departamento de Geología, Facultad de Ciencias Físicas y Matemáticas, Universidad de Chile, 2011.

Sasaki, Y.: Resolution of resistivity tomography inferred from numerical simulation, Geophys. Prospect., 40, 453–464, 1992.

Unsworth, M., Bedrosian, P., Eisel, M., Egbert, G., and Siripunvaraporn, W.: Along strike variations in the electrical structure of the San Andreas Fault at Parkfield, California, Geophys. Res. Lett. 27, 3021–3024, 2000.

Van Avendonk, H. J. A., Harding, A. J., and Orcutt, J. A.: A two-dimensional tomographic study of the Clipperton transform fault, J. Geophys. Res., 103, 17885–17899, 1998.

Vargas, G. and Rebolledo, S.: Paleosismología de la falla San Ramón e implicancias para el peligro sísmico de Santiago. XIII Congreso Geológico Chileno, Antofagasta, Chile, Meeting Abstracts 851-853, 2012.

Vera, E., Mutter, J. C., Buhl, P., Orcutt, J. A., Harding, A. J., Kappus, M. E., Detrick, R. S., and Brocher, T. M.: The Structure of 0- to 0.2-m.y.-Old Oceanic Crust at 9° N on the East Pacific Rise From Expanded Spread Profiles, J. Geophys. Res., 95, 15529–15556, doi:10.1029/JB095iB10p15529, 1990.

Zarroca, M., Bach, J., Linares, R., and Pellicer, X.: Electrical methods (VES and ERT) for identifying, mapping and monitoring different saline domains in a coastal plain region (Alt Empordà, Northern Spain), J. Hydrol., 409, 407–422, 2011.

Zhdanov, M. S.: Geophysical Electromagnetic Theory and Methods, Elsevier, 2009.